A Calculation Method of IGBT Insulation Voltages Based on Submodule Stray Capacitors in MMC

Tao Sun, Xuejun Pei, *Senior Member, IEEE*, Jiuqing Cai, Fang Wu, Youwen Zhang, and Yong Kang, *Fellow, IEEE*

***Abstract*—In practical modular multilevel converter (MMC) engineering, the dc voltage can be as high as tens to hundreds of kV, while the insulated gate bipolar transistors (IGBTs) isolation voltage is only several kV. The extreme high voltage of MMC can easily destroy the ceramic layers of the IGBT. To assess the IGBT insulation voltages and help design insulation protection measures in the early design stage of MMC, this article proposes a submodule stray capacitor based calculation method for IGBT insulation voltages. First, the switching-states and the stray capacitor model of submodules are introduced. Then, the IGBT insulation voltages are derived in detail, and the voltage characteristics under normal and fault conditions are analyzed. After that, the effect of the heatsink-to-ground capacitance on the maximum IGBT insulation voltages is discussed. The proposed method has a good accuracy with most relative errors less than 5% (calculation versus simulation) and 20% (calculation versus experiment). To protect the insulation safety of IGBTs, this article also gives a design example of the maximum heatsink-to-ground stray capacitance. The proposed method can not only guide the IGBT insulation protection design, but also provide the model reference and the heatsink-to-ground voltage estimation for the EMI researches of MMC.**

***Index Terms*—Heatsink-to-ground voltage, insulated gate bipolar transistors (IGBTs) insulation protection, IGBT insulation voltage, modular multilevel converter, submodule stray capacitor model.**

NOMENCLATURE

N	Amount of bridge-arm submodules in MMC.
U_{dc}	DC voltage of MMC.
U_{C}	Average voltage of submodule capacitors.
U_{isol}	IGBT isolation voltage.
u_{HG}	Heatsink-to-ground voltage.
u_{ins}	IGBT insulation voltage.
$u_{x\mathrm{G}}$	Voltage between the submodule's xth node and the ground, where $x = 1, 2, 3, 4$.
$u_{x\mathrm{H}}$	Voltage between the submodule's xth node and the heatsink, where $x = 1, 2, 3, 4$.
$i_{x\mathrm{H}}$	Current from the submodule's xth node into the heatsink, where $x = 1, 2, 3, 4$.
φ^{+}	Voltage between the submodule's positive input port and the ground.
φ^{-}	Voltage between the submodule's negative input port and the ground.
S	Submodule switching-state.
S_{L}	Switching-state of submodule left half-bridge.
S_{R}	Switching-state of submodule right half-bridge.
C_{C}	Collector-to-heatsink capacitance of IGBT.
C_{O}	Output-to-heatsink capacitance of IGBT.
C_{E}	Emitter-to-heatsink capacitance of IGBT.
C_{H}	Heatsink-to-ground capacitance.
$C_{x\mathrm{H}}$	Capacitance between the submodule's xth node and the heatsink, where $x = 1, 2, 3, 4$.
C_{SW}	Sum of IGBT stray capacitance in a submodule.

I. INTRODUCTION

MODULAR multilevel converter (MMC), which was proposed by Lesnicar and Marquardt [1], has become the most widely used multilevel converter in high voltage direct current transmission engineering [2], [3]. MMC not only inherits the common advantages of multilevel converters, but also has its unique advantages such as modular production and easy replacement [4], [5]. Existing researches on MMC focus on the submodule topology, modulation algorithms, and control methods. However, the insulation issue of the insulated gate bipolar transistors (IGBT) in MMC is rarely noticed. Fig. 1 shows the inner structure of a wire-bond half-bridge IGBT module. This IGBT module comprises a plastic casing, three electrode ports, four driver ports, and a multilayer structure. Thereinto, the multilayer structure is the core component. For the convenience of explanation, the multilayer structure is simplified into three layers: 1) the copper layer (conductive), 2) the ceramic layer (insulating), and 3) the metal baseplate (conductive). The three layers form an equivalent parallel-plate capacitor. The switch chips and the electrode ports are welded on the top of the copper layer. The metal baseplate is placed on the heatsink for heat dissipation.

Manuscript received 18 May 2024; revised 2 July 2024; accepted 5 August 2024. Date of publication 14 August 2024; date of current version 7 October 2024. This work was supported in part by the Delta Power Electronics Science and Education Development Program of Delta Group under Grant DREK2023002, and in part by the National Natural Science Foundation of China under Grant 52377187 and Grant 51977091. Recommended for publication by Associate Editor S. Mekhilef. *(Corresponding author: Xuejun Pei.)*

Tao Sun, Xuejun Pei, Youwen Zhang, and Yong Kang are with the Power Electronics and Energy Management Key Laboratory, Ministry of Education of China, Huazhong University of Science and Technology, Wuhan 430074, China (e-mail: d202080595@hust.edu.cn; ppei215@mail.hust.edu.cn; d202080609@hust.edu.cn; ykang@hust.edu.cn).

Jiuqing Cai and Fang Wu are with the Wuhan Second Ship Design and Research Institute, Wuhan 430202, China (e-mail: d201277335@alumni.hust.edu.cn; d201377552@alumni.edu.cn).

Color versions of one or more figures in this article are available at https://doi.org/10.1109/TPEL.2024.3443472.

Digital Object Identifier 10.1109/TPEL.2024.3443472

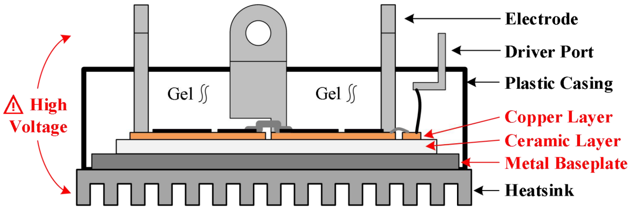

Fig. 1. Inner structure of wire-bond half-bridge IGBT module.

In low-voltage converters, the IGBT modules are usually placed on a common heatsink, and the heatsink is mounted on the grounded chassis [6]. In this situation, the voltages on the ceramic layer are the voltages between the electrodes and the ground. Generally, the isolation voltage of the ceramic layer is several kV, far greater than the input voltage. Therefore, there is no IGBT insulation problem in low-voltage converters. However, in high-voltage converters such as MMCs, the voltages between the electrodes and the ground can be extremely high (tens to hundreds of kV). Such high voltage can easily destroy the ceramic layers. Therefore, the heatsinks in high-voltage converters cannot be grounded. Instead, there must be some insulating materials between the heatsinks and the chassis to share the high voltage [7], [8], [9]. Moreover, considering that there are numerous submodules in MMC, it is impossible to place all IGBT modules one common heatsink. Hence, each submodule has its own heatsink. The large amount of floating heatsinks with different potentials brings about another problem: the insulation voltages on the ceramic layers of IGBT modules become unknown, so engineers can not judge whether the IGBT modules are safe or not. Obviously, knowing the real-time IGBT insulation voltages is essential to protect the IGBT modules in MMC.

The existing literature related to the IGBT insulation voltages only focuses on the breakdown voltages rather than real-time voltage. In the existing literature, the way to assess the insulation voltages of IGBT modules includes simulation and experiment methods. The simulation method depends on the finite element analysis (FEA) or multiphysics simulation software. One approach is to simulate the electrical field distribution of the ceramic substrate [10], [11], [12]. When the simulated electrical field strength exceeds the breakdown field strength of the ceramic layer, it means that the given excitation voltage will lead to IGBT insulation breakdown. However, this method can only obtain the breakdown voltage rather than real-time insulation voltage. Another approach is to simulate the partial discharge (PD) of the void or gel by multiphysics software [13], [14]. When the PD phenomenon is observed, the insulation deterioration has begun. Usually, the simulation models are very complicated with a great many parameters. Compared to simulation methods, the experiment methods are more employed. Thereinto, the PD test is the most widely adopted method [15], [16], [17], [18], [19]. The idea of the PD test is observing the PD phenomenon by repeatedly exerting voltages on the ceramic layer. Similar to the first simulation method, the PD test can only obtain the breakdown voltage.

To some extent, obtaining the real-time IGBT insulation voltages is a condition monitoring problem. However, the existing researches on IGBT condition monitoring measure the ON-state voltage, gate-emitter voltage, junction temperature, and switching time while the monitoring of IGBT insulation voltage has not been reported yet. Generally, the way to monitor an electrical quantity includes measured method [20], [21], [22], [23] and inferred method [24], [25]. The measured method needs additional sensors and isolated sampling circuits to measure the real-time conditions, which increases the system complexity. Compared to the measured method, the inferred method is a convenient choice, since most parameters are already known. Inspired by the inferred method, this article proposes a calculation method to obtain the IGBT insulation voltages based on the switching-states and stray capacitors of submodules. Different from the time-consuming simulation methods and destructive high voltage experiment methods, the proposed method can assess the IGBT insulation voltages fast and accurately. The comparison of the proposed method and the existing literature is listed in Table I.

The rest of this article is organized as follows. Section II introduces the submodule switching-states and the submodule stray capacitor model. According to the switching-states and stray capacitor model, the IGBT insulation voltages are derived in Section III, and the effects of working conditions are discussed. Then, the maximum IGBT insulation voltages are analyzed in Section IV. Section V verifies the accuracy of the proposed method. Based on the maximum IGBT insulation voltages, an example is given in Section VI to design the maximum heatsink-to-ground capacitance. Finally, Section VII concludes this article.

II. SWITCHING-STATES AND STRAY CAPACITOR MODEL OF SUBMODULES IN MMC

The switching-states and stray capacitors of submodules are two critical factors to calculate the IGBT insulation voltages. This section introduces the possible switching-states and stray capacitor model of submodules, which will be used for the voltage derivation in Section III.

A. *Switching-States of Submodules in MMC*

Fig. 2 shows the main circuit of a three-phase MMC. Each phase includes an upper/positive bridge-arm (marked as "p") and a lower/negative bridge-arm (marked as "n"). In each bridge-arm, there are N submodules and an mH-level inductor in series. The submodules can be half-bridge submodules (HBSMs), full-bridge submodules (FBSMs), or the hybrid of these two types. The difference between these two types is that the FBSM can output negative voltage in some special situations. By changing the number of ON-state submodules, the bridge-arm outputs different levels of voltages. In general, to avoid large circulation currents among three phases, there should always be N ON-state submodules in each phase. The dc voltage U_{dc} and the submodule capacitor average voltage U_{C} satisfy the relation as follows:

$$U_{\mathrm{dc}} = NU_{\mathrm{C}}. \tag{1}$$

TABLE I
COMPARISON OF THE PROPOSED METHOD AND THE EXISTING LITERATURE

Reference	Type	Observed object	Description	Real-time	Benefits	Drawbacks
[10], [11]	Simulation	Electrical field, breakdown voltage	FEA simulation	No	• Parameter adjustable • Repeatable, safe	• Complicated model • Many parameters • Time-consuming
[12]			Numerical simulation			
[13], [14]		Insulation voltage	Multiphysics simulation	Yes		
[15], [16]	Measurement	Breakdown voltage	Ac voltage PD test	No	• High accuracy • Strong credibility	• Semidestructive • High voltage danger • Specific condition
[17]			Dc voltage PD test			
[18], [19]			Square-wave voltage PD test			
[20]		On-state voltage	Measured condition monitoring	Yes	• High resolution • Condition-independent	• Additional sensors • Isolation issue
[21]		Gate-emitter voltage				
[22]		Junction temperature				
[23]		Switching time				
[24], [25]	Calculation	On-state voltage	Inferred condition monitoring	Yes	• Sensor reduction	• Condition-dependent
This paper	Calculation	Insulation voltage	Stray capacitor based Calculation	Yes	• Fast, safe, convenient • Condition-independent	• Model-dependent

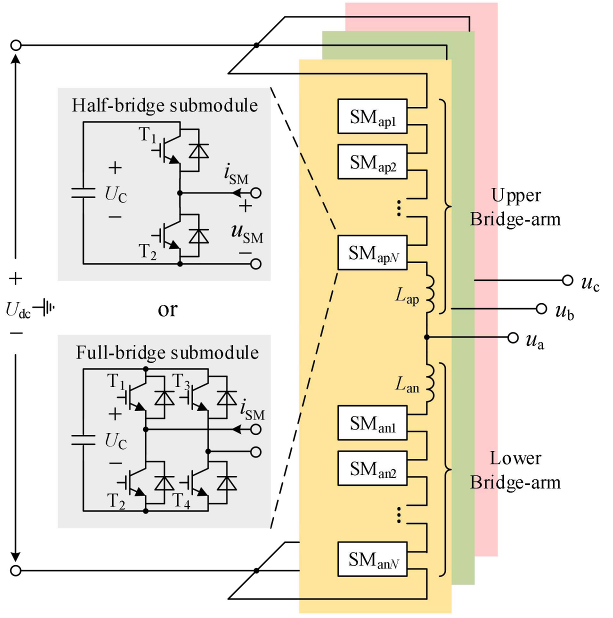

Fig. 2. Main circuit of three-phase MMC.

TABLE II
SUBMODULE SWITCHING-STATES AND CORRESPONDING OUTPUT VOLTAGES

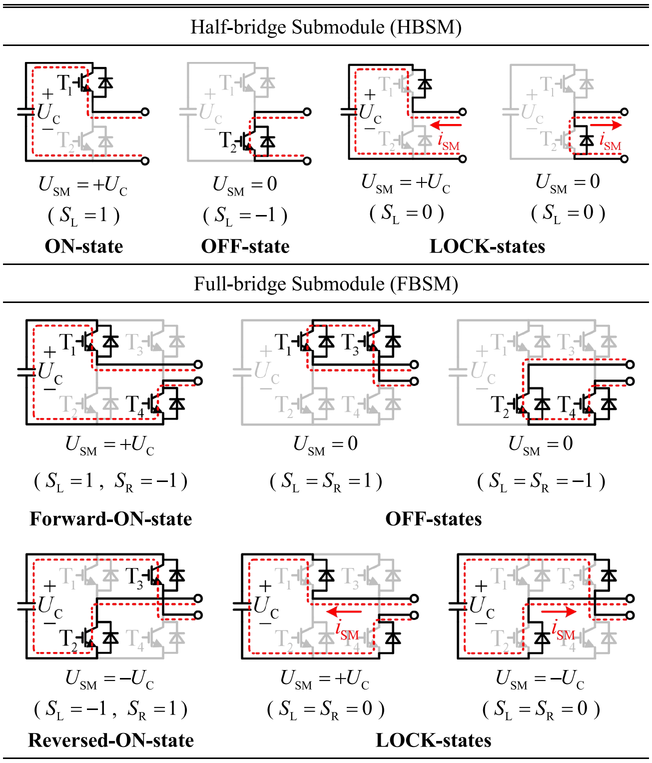
Half-bridge Submodule (HBSM)

$U_{SM}=+U_C$ ($S_L=1$) **ON-state**

$U_{SM}=0$ ($S_L=-1$) **OFF-state**

$U_{SM}=+U_C$ ($S_L=0$); $U_{SM}=0$ ($S_L=0$) **LOCK-states**

Full-bridge Submodule (FBSM)

$U_{SM}=+U_C$ ($S_L=1$, $S_R=-1$) **Forward-ON-state**

$U_{SM}=0$ ($S_L=S_R=1$); $U_{SM}=0$ ($S_L=S_R=-1$) **OFF-states**

$U_{SM}=-U_C$ ($S_L=-1$, $S_R=1$) **Reversed-ON-state**

$U_{SM}=+U_C$ ($S_L=S_R=0$); $U_{SM}=-U_C$ ($S_L=S_R=0$) **LOCK-states**

Take the FBSMs for example. Define the switching-state of the left half-bridge in an FBSM as

$$S_L = \begin{cases} 1, & \text{when } T_1 \text{ is on and } T_2 \text{ is off} \\ 0, & \text{when } T_1 \text{ and } T_2 \text{ are both off} \\ -1, & \text{when } T_1 \text{ is off and } T_2 \text{ is on.} \end{cases} \quad (2)$$

Similarly, the switching-state of the right half-bridge is

$$S_R = \begin{cases} 1, & \text{when } T_3 \text{ is on and } T_4 \text{ is off} \\ 0, & \text{when } T_3 \text{ and } T_4 \text{ are both off} \\ -1, & \text{when } T_3 \text{ is off and } T_4 \text{ is on.} \end{cases} \quad (3)$$

Then, the submodule switching-state S can be represented as

$$S = \frac{1}{2}(S_L - S_R) = \begin{cases} 1, & \text{when the FBSM outputs } +U_C \\ 0, & \text{when the FBSM outputs 0} \\ -1, & \text{when the FBSM outputs } -U_C. \end{cases} \quad (4)$$

Table II lists the submodule switching-states and the corresponding submodule output voltages. It it noted that the submodule output voltages of LOCK-states depend on the instantaneous direction of the bridge-arm current i_{SM}. When a LOCK-state submodule outputs $+U_C$, its equivalent switching-state is 1; when a LOCK-state submodule outputs $-U_C$, its equivalent switching-state is −1. For a HBSM, it can be seen as a special kind of FBSM whose T_3 is always OFF and T_4 always ON. This article mainly focuses on the case of FBSMs. The case of HBSMs will be given in Appendix.

The submodule switching-states are effected by the adopted modulation method. For high-voltage MMCs, the most widely

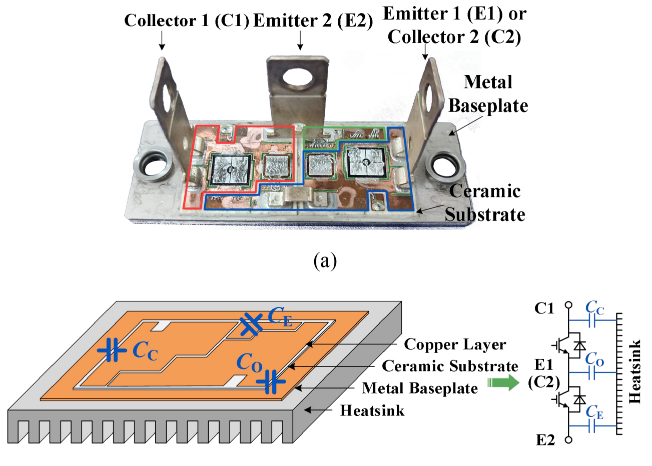

(a)

(b)

Fig. 3. Half-bridge IGBT module. (a) Inner structure of SKM100GB12 V. (b) Simplified stray capacitor model.

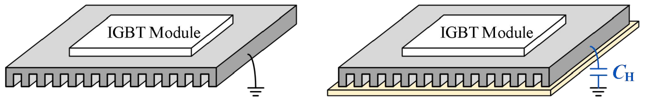

(a) (b)

Fig. 4. Heatsink installation manners. (a) Connected to metal chassis of low-voltage converters. (b) Isolated to metal chassis of MMC.

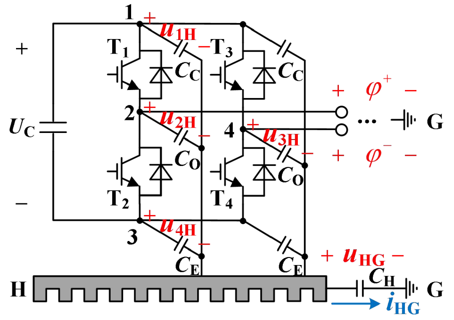

Fig. 5. Stray capacitor model of FBSM.

used modulation method is the nearest-level modulation (NLM). While for middle and low voltage MMCs, the multicarrier based modulation methods can also be used, such as the carrier phase shift pulsewidth modulation (CPS-PWM). The IGBT insulation voltage characteristics under different modulation methods will be analyzed in Section III.

B. Stray Capacitor Model of Submodules in MMC

Apart from switching-states, the submodule stray capacitors are also critical factors that affect the IGBT insulation voltages. There are two kinds of stray capacitors in a submodule: one is the stray capacitors of IGBT modules, and the another is the stray capacitors of heatsinks.

The stray capacitors of IGBT modules include the junction capacitors and the stray capacitors between the electrodes and the metal baseplate. The junction capacitors affect the dynamic characteristics of switching processes. However, the calculated voltages in this article are steady-state voltages in different switching-states. Hence, the junction capacitors are neglected for model simplification. Fig. 3(a) depicts the inner structure of a half-bridge IGBT module. The IGBT module is stacked up by several layers. Most layers are conductive, while the ceramic layer (made of Al_2O_3, AlN, or Si_3N_4 [26]) is insulating. Usually, the isolation voltage of the ceramic layer is several kV. If the voltage on the ceramic layer exceeds the isolation voltage, the ceramic layer will insulation break down.

Fig. 3(b) shows the simplified inner structure of an IGBT module. The copper layer (conductive), the ceramic layer (insulating), and the metal baseplate (conductive) form three parallel-plate stray capacitors. According to the parallel-plate capacitor theory, the capacitance of the parallel-plate capacitor C_{PPC} is relevant to the dielectric constant ε of the ceramic layer, the overlapping area A of three layers and the thickness d of the ceramic layer, i.e.,

$$C_{\mathrm{PPC}} = \frac{\varepsilon A}{d}. \tag{5}$$

As shown in Fig. 3, the copper layer is divided into three zones, which are respectively welded to the three electrodes of the IGBT module. The upper IGBT collector (C1) and the upper freewheeling diode (FWD) cathode are welded in the red zone. The upper IGBT emitter (E1) and the upper FWD anode as well as the lower IGBT collector (C2) and the lower FWD cathode are welded in the blue zone. The lower IGBT emitter (E2) and the lower FWD anode are welded in the green zone. The metal baseplate and the heatsink are fixed together by bolts, so they can be seen as equipotential. Obviously, there are three stray capacitors between the IGBT electrodes and the heatsink: C_{C}, C_{O}, and C_{E}, where C_{C} is the capacitance of the red zone, C_{O} is the capacitance of the blue zone, and C_{E} is the capacitance of the green zone.

The stray capacitors of heatsinks are also important factors that influence IGBT insulation voltages. As aforementioned in Introduction, the heatsink in a low-voltage converter is directly connected to the metal chassis, as shown in Fig. 4(a). While for a high-voltage converter, the heatsinks can not be directly mounted on the metal chassis. To protect the IGBTs from insulation breakdown, some insulating materials should be added between the heatsinks and the metal chassis to share the insulation voltage, as shown in Fig. 4(b). The added insulating materials form a stray capacitor C_{H} between the heatsink and the grounded metal chassis [27]. It is noted that C_{H} also has great influences on the conducted electromagnetic interference (EMI) of MMC, since the heatsinks are important conducting paths of the common-mode current in MMC [28].

The complete stray capacitor model of an FBSM can be obtained by assembling the stray capacitors above, as shown in Fig. 5. It is noted that each submodules has its own heatsink. In Fig. 5, φ^+ is the voltage of the positive input port to the ground, while φ^- is the voltage of the negative input port to the ground. $u_{1\mathrm{H}}$–$u_{4\mathrm{H}}$ are the voltages across the IGBT stray capacitors, i.e., the IGBT insulation voltages, and u_{HG} is the heatsink-to-ground voltage. i_{HG} is the common-mode current from the submodule heatsink into the grounded metal chassis.

III. CALCULATION OF IGBT INSULATION VOLTAGES BASED ON SUBMODULE SWITCHING-STATES AND STRAY CAPACITORS

Based on the submodule switching-states and the stray capacitor model obtained in Section II, the expressions of IGBT insulation voltages can be derived. This section only discusses FBSMs. The case of HBSMs is given in Appendix.

A. Calculation of IGBT Insulation Voltages

In Fig. 5, to calculate the IGBT insulation voltages, it is necessary to firstly calculate the electrode-to-ground voltages $u_{1\mathrm{G}}$–$u_{4\mathrm{G}}$. Then, the heatsink-to-ground voltage u_{HG} can be obtained by applying the Kirchhoff's current law. Finally, the IGBT insulation voltages are obtained by subtracting u_{HG} from $u_{1\mathrm{G}}$–$u_{4\mathrm{G}}$. The detailed derivation processes are as follows.

Assume the submodule capacitor voltage to be constant as U_{C}. For an FBSM in the upper bridge-arm, its electrode-to-ground voltages can be represented as

$$\begin{cases} u_{1\mathrm{G}} = \varphi^{+} + (1 - S_{\mathrm{L}})\,\frac{U_{\mathrm{C}}}{2}, & u_{2\mathrm{G}} = \varphi^{+} \\ u_{3\mathrm{G}} = \varphi^{+} - (1 + S_{\mathrm{L}})\,\frac{U_{\mathrm{C}}}{2}, & u_{4\mathrm{G}} = \varphi^{+} - (S_{\mathrm{L}} - S_{\mathrm{R}})\,\frac{U_{\mathrm{C}}}{2}. \end{cases} \tag{6}$$

According to the Kirchhoff's voltage law, the IGBT insulation voltages $u_{1\mathrm{H}}$–$u_{4\mathrm{H}}$ can be calculated as

$$u_{x\mathrm{H}} = u_{x\mathrm{G}} - u_{\mathrm{HG}} \tag{7}$$

where *x* denotes the *x*th electrode in the FBSM, $x = 1, 2, 3, 4$.

According to the capacitor volt-ampere relation, the current from the *x*th electrode into the heatsink is calculated as

$$i_{x\mathrm{H}} = C_{x\mathrm{H}}\frac{\mathrm{d}u_{x\mathrm{H}}}{\mathrm{d}t} = C_{x\mathrm{H}}\frac{\mathrm{d}}{\mathrm{d}t}\left(u_{x\mathrm{G}} - u_{\mathrm{HG}}\right) \tag{8}$$

where $C_{1\mathrm{H}} = 2C_{\mathrm{C}}$, $C_{2\mathrm{H}} = C_{4\mathrm{H}} = C_{\mathrm{O}}$, and $C_{3\mathrm{H}} = 2C_{\mathrm{E}}$. $C_{1\mathrm{H}}$–$C_{4\mathrm{H}}$ denote the total capacitance between the *x*th electrode and the heatsink. According to the Kirchhoff's current law, the total current i_{HG} from the heatsink into the ground is calculated as

$$i_{\mathrm{HG}} = C_{\mathrm{H}}\frac{\mathrm{d}u_{\mathrm{HG}}}{\mathrm{d}t} = i_{1\mathrm{H}} + i_{2\mathrm{H}} + i_{3\mathrm{H}} + i_{4\mathrm{H}}. \tag{9}$$

By combining (2)–(4) and (6)–(8), (9) is simplified as

$$\frac{\mathrm{d}u_{\mathrm{HG}}}{\mathrm{d}t} = C_1\frac{\mathrm{d}\varphi^{+}}{\mathrm{d}t} - C_2U_{\mathrm{C}}\frac{\mathrm{d}S_{\mathrm{L}}}{\mathrm{d}t} + C_3U_{\mathrm{C}}\frac{\mathrm{d}S_{\mathrm{R}}}{\mathrm{d}t} \tag{10}$$

where $C_1 = \frac{C_{\mathrm{SW}}}{C_{\mathrm{SW}}+C_{\mathrm{H}}}$, $C_2 = \frac{1}{2}\,\frac{C_{\mathrm{SW}}-C_{\mathrm{O}}}{C_{\mathrm{SW}}+C_{\mathrm{H}}}$, $C_3 = \frac{1}{2}\,\frac{C_{\mathrm{O}}}{C_{\mathrm{SW}}+C_{\mathrm{H}}}$, and $C_{\mathrm{SW}} = 2(C_{\mathrm{C}} + C_{\mathrm{O}} + C_{\mathrm{E}})$. For the ith FBSM in the upper bridge-arm $\mathrm{SM}_{\mathrm{p}i}$, its positive input port are connected with the negative input port of $\mathrm{SM}_{\mathrm{p}(i-1)}$, i.e., $\varphi^{+}_{\mathrm{p}i} = \varphi^{-}_{\mathrm{p}(i-1)}$. Considering (1), then

$$\varphi^{+}_{\mathrm{p}i} = \frac{U_{\mathrm{dc}}}{2} - \left(\sum_{k=1}^{i-1} S_{\mathrm{p}k}\right)U_{\mathrm{C}} = \left(\frac{N}{2} - \sum_{k=1}^{i-1} S_{\mathrm{p}k}\right)U_{\mathrm{C}}. \tag{11}$$

Substitute (11) into (10), then

$$\frac{\mathrm{d}}{\mathrm{d}t}\left(\frac{u_{\mathrm{HG,p}i}}{U_{\mathrm{C}}}\right) = -C_1\frac{\mathrm{d}}{\mathrm{d}t}\left(\sum_{k=1}^{i-1} S_{\mathrm{p}k}\right) - C_2\frac{\mathrm{d}S_{\mathrm{L,p}i}}{\mathrm{d}t} + C_3\frac{\mathrm{d}S_{\mathrm{R,p}i}}{\mathrm{d}t}. \tag{12}$$

For the convenience of expression, the voltages in the rest part of this article are all normalized as per unit values unless particularly stated. The reference voltage of the per unit values is U_{C}. By integrating (10), the heatsink-to-ground voltage of $\mathrm{SM}_{\mathrm{p}i}$ can be calculated as (see Appendix)

$$u^{\mathrm{p.u.}}_{\mathrm{HG,p}i} = -C_1\sum_{k=1}^{i-1} S_{\mathrm{p}k} - C_2S_{\mathrm{L,p}i} + C_3S_{\mathrm{R,p}i} + \frac{i}{2}C_1 - \frac{1}{2}\frac{2C_{\mathrm{E}} + C_{\mathrm{O}}}{C_{\mathrm{SW}} + C_{\mathrm{H}}}. \tag{13}$$

Finally, the IGBT insulation voltages can be obtained by subtracting (13) from (6). It is worth mentioning that only the IGBT insulation voltage that has the largest amplitude in $u_{1\mathrm{H}}$–$u_{4\mathrm{H}}$ need to be considered. For an upper bridge-arm FBSM, $u_{1\mathrm{H}}$ has the largest amplitude. Therefore, the IGBT insulation voltage $u^{\mathrm{p.u.}}_{\mathrm{ins}}$ of $\mathrm{SM}_{\mathrm{p}i}$ is calculated as

$$\begin{aligned} u^{\mathrm{p.u.}}_{\mathrm{ins,p}i} &= u^{\mathrm{p.u.}}_{1\mathrm{G,p}i} - u^{\mathrm{p.u.}}_{\mathrm{HG,p}i} \\ &= \underbrace{-\left(1 - C_1\right)\sum\nolimits_{k=1}^{i-1} S_{\mathrm{p}k}}_{\substack{\text{relavant to the switching}-\\ \text{states of other submodules}}} \underbrace{-\left(\frac{1}{2} - C_2\right)S_{\mathrm{L,p}i} - C_3S_{\mathrm{R,p}i}}_{\substack{\text{relavant to the switching}-\text{state}\\ \text{of the observed submodule}}} \\ &\quad \underbrace{-\frac{i}{2}C_1}_{\substack{\text{relavant to the}\\ \text{submodule location}}} + \underbrace{\frac{N+1}{2}}_{\substack{\text{relavant to the amount}\\ \text{of bridge}-\text{arm submodules}}} \\ &\quad + \underbrace{\frac{1}{2}\frac{2C_{\mathrm{E}} + C_{\mathrm{O}}}{C_{\mathrm{SW}} + C_{\mathrm{H}}}}_{\substack{\text{relavant to the circuit}\\ \text{component parameters}}}. \end{aligned} \tag{14}$$

The derivation processes of lower bridge-arm submodules are similar. For the jth FBSM in the lower bridge-arm $\mathrm{SM}_{\mathrm{n}j}$, its IGBT insulation voltage is calculated as

$$\begin{aligned} u^{\mathrm{p.u.}}_{\mathrm{ins,n}j} = u^{\mathrm{p.u.}}_{3\mathrm{G,n}j} - u^{\mathrm{p.u.}}_{\mathrm{HG,n}j} &= (1 - C_1)\sum_{l=j+1}^{N} S_{\mathrm{n}l} - C_3S_{\mathrm{L,n}j} \\ &\quad - \left(\frac{1}{2} - C_2\right)S_{\mathrm{R,n}j} \\ &\quad + \frac{m}{2}C_1 - \frac{N+1}{2} - \frac{1}{2}\frac{2C_{\mathrm{C}} + C_{\mathrm{O}}}{C_{\mathrm{SW}} + C_{\mathrm{H}}} \end{aligned} \tag{15}$$

where $m = N - j + 1$. Obviously, when $i + j = N - 1$, $\mathrm{SM}_{\mathrm{p}i}$ and $\mathrm{SM}_{\mathrm{n}j}$ are symmetry about the phase midpoint. The voltage expressions of $\mathrm{SM}_{\mathrm{p}i}$ and $\mathrm{SM}_{\mathrm{n}m}$ are symmetry as well.

It can be seen from (14) and (15) that the IGBT insulation voltages are relevant to five factors: 1) the switching-states of

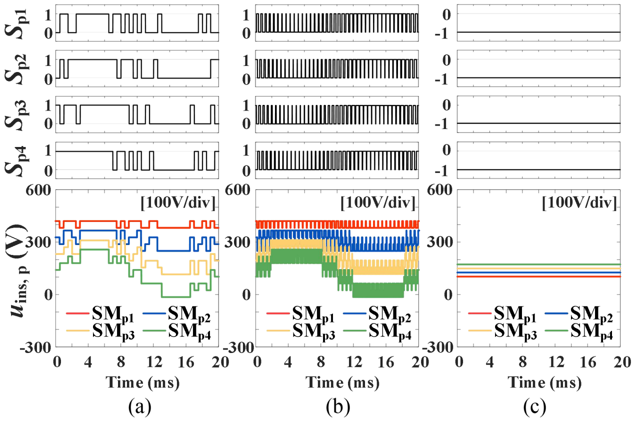

(a) (b) (c)

Fig. 6. IGBT insulation voltages under different conditions ($U_{\mathrm{dc}} = 750$ V, $N = 4$, $C_{\mathrm{H}} = 500$ pF). (a) NLM. (b) CPS-PWM. (c) DC short-circuit fault.

other submodules; 2) the switching-state of the observed submodule; 3) the submodule location; 4) the amount of bridge-arm submodules; 5) the circuit component parameters.

Generally, the amount of bridge-arm submodules N, the IGBT stray capacitance C_{C}, C_{O}, C_{E}, and the submodule locations can not be changed. Therefore, the IGBT insulation voltages are mainly determined by the submodule switching-states and the heatsink-to-ground capacitance.

B. IGBT Insulation Voltage Characteristics Under Normal and DC Short-Circuit Fault Conditions

The submodule switching-states have great effects on IGBT insulation voltages. Under normal conditions, the switching-states are determined by the modulation methods. While under fault conditions, all submodules are in LOCK-states.

Fig. 6(a) shows the submodule switching-states and IGBT insulation voltages under NLM. The NLM only determines the number of ON-state submodules in each bridge-arm. If $i_{\mathrm{SM}} \geq 0$, the submodules having the smaller capacitor voltages are prior to be turned ON; if $i_{\mathrm{SM}} < 0$, the case is contrary. Fig. 6(b) shows the case under CPS-PWM. Compared to NLM, the switching frequency of CPS-PWM is much larger than NLM. However, the maximum voltages of these two modulation methods are the same. This is because the switching-state combination that has the maximum voltages appears in both modulation methods. It can also be observed that the submodules closer to dc buses have larger IGBT insulation voltages. Therefore, SM$_{\mathrm{p}1}$ and SM$_{\mathrm{n}N}$ are the most dangerous submodules under normal conditions.

Fig. 6(c) shows the submodule switching-states and IGBT insulation voltages under dc short-circuit fault condition. In general, the ac ports of MMC are connected to the ac grid. When there is a dc short-circuit fault, the IGBTs are all turned OFF and all submodules are in LOCK-states. Under this condition, the switching-states of the upper bridge-arm submodules are all -1, while the switching-states of the lower bridge-arm submodules are all $+1$. The dc voltage becomes zero when the dc short-circuit fault occurs, making the IGBT insulation voltages smaller than normal conditions.

TABLE III
SWITCHING-STATE VARIATIONS AND CORRESPONDING VOLTAGE JUMPS

Switching-State Variation		Voltage Jump $\Delta u_{\mathrm{ins},\,pi}^{\mathrm{p.u.}}$	Voltage Jump $\Delta u_{\mathrm{ins},\,nj}^{\mathrm{p.u.}}$
$\Delta\sum_{k=1}^{i-1} S_{pk}$ or $\Delta\sum_{l=j+1}^{N} S_{nl}$	+1	$-(1-C_1)<0$	$+(1-C_1)>0$
	−1	$+(1-C_1)>0$	$-(1-C_1)<0$
$\Delta S_{\mathrm{L},\,pi}$ or $\Delta S_{\mathrm{L},\,nj}$	+1	$-\left(\frac{1}{2}-C_2\right)<0$	$-C_3<0$
	−1	$+\left(\frac{1}{2}-C_2\right)>0$	$+C_3>0$
$\Delta S_{\mathrm{R},\,pi}$ or $\Delta S_{\mathrm{R},\,nj}$	+1	$-C_3<0$	$-\left(\frac{1}{2}-C_2\right)<0$
	−1	$+C_3>0$	$+\left(\frac{1}{2}-C_2\right)>0$

To ensure the absolute safety of IGBTs, it is essential to find the theoretical maximum IGBT insulation voltages. However, the maximum IGBT insulation voltages under normal conditions are not the theoretical maximum voltages. Under some special conditions, the maximum IGBT insulation voltages can be greater than normal conditions.

IV. ANALYSIS ON MAXIMUM IGBT INSULATION VOLTAGES AND EFFECT OF HEATSINK-TO-GROUND CAPACITANCE

The working condition of MMC has great effects on IGBT insulation voltages. However, it is difficult to consider all kinds of working conditions. As aforementioned, it is critical to find out the submodule switching-state combination that has the maximum IGBT insulation voltages.

A. Analysis on Maximum IGBT Insulation Voltages

By observing (14) and (15), it can be seen that the last three items on the right side of (14) and (15) are fixed when C_{H} is certain. At this time, the maximum IGBT insulation voltages $u_{\mathrm{ins,\,max}}^{\mathrm{p.u.}}$ can be deduced according to the voltage jumps caused by the variations of submodule switching-states. Table III lists the switching-state variations (ΔS, ΔS_{L}, and ΔS_{R}) and the corresponding voltage jumps $\Delta u_{\mathrm{ins}}^{\mathrm{p.u.}}$.

It is noted that the mentioned maximum IGBT insulation voltage in this article is actually the maximum absolute value $|u_{\mathrm{ins}}^{\mathrm{p.u.}}|_{\max}$. Considering that $u_{\mathrm{ins,\ p}i}^{\mathrm{p.u.}} > 0$ and $u_{\mathrm{ins,\ p}i}^{\mathrm{p.u.}} < 0$, to make $|u_{\mathrm{ins,\ p}i}^{\mathrm{p.u.}}|$ and $|u_{\mathrm{ins,\ n}j}^{\mathrm{p.u.}}|$ as larger as possible: 1) $\Delta\sum_{k=1}^{i-1} S_{\mathrm{p}k}$, $\Delta S_{\mathrm{L,\ p}i}$ and $\Delta S_{\mathrm{R,\ p}i}$ should be all negative; 2) $\Delta\sum_{l=j+1}^{N} S_{\mathrm{n}l}$ should be negative, while $\Delta S_{\mathrm{L,\ n}j}$ and $\Delta S_{\mathrm{R,\ n}j}$ should be both positive.

Based on the above analysis, when SM$_{\mathrm{p}1}$, SM$_{\mathrm{p}2}$, …, SM$_{\mathrm{p}(i-1)}$ all output $-U_{\mathrm{C}}$ and SM$_{\mathrm{p}i}$ outputs zero, $|u_{\mathrm{ins,\ p}i}^{\mathrm{p.u.}}|$ has its maximum value; when SM$_{\mathrm{n}(j+1)}$, SM$_{\mathrm{n}(j+2)}$, …, SM$_{\mathrm{n}N}$ all output $-U_{\mathrm{C}}$ and SM$_{\mathrm{n}j}$ outputs zero, $|u_{\mathrm{ins,\ n}j}^{\mathrm{p.u.}}|$ has its maximum value.

Fig. 7 shows the switching-states when $|u_{\mathrm{ins,\ p}i}^{\mathrm{p.u.}}|$ and $|u_{\mathrm{ins,\ n}j}^{\mathrm{p.u.}}|$ get their maximum values. Substitute the switching-states in Fig. 7 into (14), (15), the maximum IGBT insulation voltages of

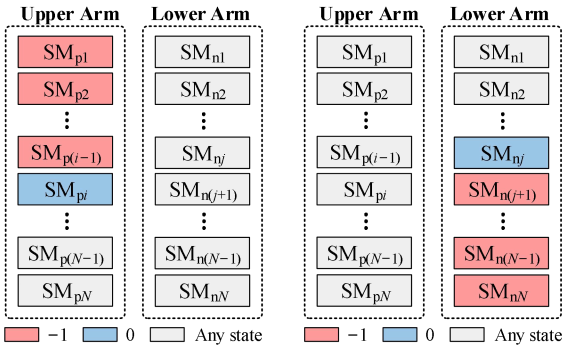

(a) (b)

Fig. 7. Submodule switching-states. (a) When $|u^{\text{p.u.}}_{\text{ins, }pi}|$ get its maximum value. (b) When $|u^{\text{p.u.}}_{\text{ins, }nj}|$ get its maximum value.

SM$_{\text{p}i}$ and SM$_{\text{n}j}$ can, then, be obtained as (note: $m = N - j + 1$)

$$\begin{cases} \left|u^{\text{p.u.}}_{\text{ins,p}i}\right|_{\max} = \left(1 - \frac{3i}{2}\right) C_1 + i + \frac{N}{2} + \frac{1}{2}\left(\frac{C_{\text{O}} - 2C_{\text{C}}}{C_{\text{SW}} + C_{\text{H}}}\right) \\ \left|u^{\text{p.u.}}_{\text{ins,n}j}\right|_{\max} = \left(1 - \frac{3m}{2}\right) C_1 + m + \frac{N}{2} + \frac{1}{2}\left(\frac{C_{\text{O}} - 2C_{\text{E}}}{C_{\text{SW}} + C_{\text{H}}}\right). \end{cases} \tag{16}$$

The submodule switching-states in Fig. 7 are most likely to appear when the MMC is working in overmodulation mode [29]. Under this condition, the submodules in one of the bridge-arms all output $-U_{\text{C}}$ and the amplitude of ac voltage can be up to $1.5U_{\text{dc}}$. To protect the insulation safety of IGBTs, the switching-states in Fig. 7 should be avoided as possible.

If the overmodulation mode is not adopted in MMC, then the bridge-arm voltage is limited within 0 to U_{dc}. Under this condition, there can be at most $N/2$ reversed-ON-state submodules in each bridge-arm. Therefore, SM$_{\text{p}(N/2+1)}$ and SM$_{\text{n}(N/2)}$ are the most dangerous submodules, of which the maximum IGBT insulation voltages are calculated as

$$\begin{cases} \left|u^{\text{p.u.}}_{\text{ins,p}(N/2+1)}\right|_{\max} = -\left(\frac{1}{2} + \frac{3N}{4}\right) C_1 + N + 1 \\ \qquad + \frac{1}{2}\left(\frac{C_{\text{O}} - 2C_{\text{C}}}{C_{\text{SW}} + C_{\text{H}}}\right) \\ \left|u^{\text{p.u.}}_{\text{ins,n}(N/2)}\right|_{\max} = -\left(\frac{1}{2} + \frac{3N}{4}\right) C_1 + N + 1 \\ \qquad + \frac{1}{2}\left(\frac{C_{\text{O}} - 2C_{\text{E}}}{C_{\text{SW}} + C_{\text{H}}}\right). \end{cases} \tag{17}$$

B. *Effect of Heatsink-to-Ground Capacitance*

According to (16), the maximum IGBT insulation voltages are influenced by the submodule locations and the heatsink-to-ground capacitance. Fig. 8 demonstrates the maximum IGBT insulation voltages when C_{H} varies. The voltage difference $\Delta u^{\text{p.u.}}_{\text{ins}}$ between two adjacent submodules is calculated as

$$\begin{cases} \Delta u^{\text{p.u.}}_{\text{ins,p}} = \left|u^{\text{p.u.}}_{\text{ins,p}(i+1)}\right|_{\max} - \left|u^{\text{p.u.}}_{\text{ins,p}i}\right|_{\max} = 1 - \frac{3}{2}C_1 \\ \Delta u^{\text{p.u.}}_{\text{ins,n}} = \left|u^{\text{p.u.}}_{\text{ins,n}(j+1)}\right|_{\max} - \left|u^{\text{p.u.}}_{\text{ins,n}j}\right|_{\max} = -\left(1 - \frac{3}{2}C_1\right). \end{cases} \tag{18}$$

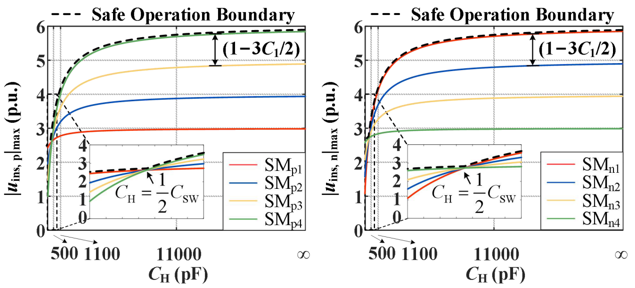

(a) (b)

Fig. 8. Maximum IGBT insulation voltages when C_{H} varies. (a) Upper bridge-arm submodules. (b) Lower bridge-arm submodules.

When $C_{\text{H}} = 0$, the heatsinks are fully floating to the ground, and the maximum IGBT insulation voltages are calculated as

$$\begin{cases} \left|u^{\text{p.u.}}_{\text{ins,p}i}\right|^{C_{\text{H}}=0}_{\max} = 1 - \frac{i}{2} + \frac{N}{2} + \frac{1}{2}\left(\frac{C_{\text{O}} - 2C_{\text{C}}}{C_{\text{SW}}}\right) \\ \left|u^{\text{p.u.}}_{\text{ins,n}j}\right|^{C_{\text{H}}=0}_{\max} = 1 - \frac{m}{2} + \frac{N}{2} + \frac{1}{2}\left(\frac{C_{\text{O}} - 2C_{\text{E}}}{C_{\text{SW}}}\right). \end{cases} \tag{19}$$

As C_{H} gradually increases, there is a critical value $C_{\text{H}} = \frac{1}{2}C_{\text{SW}}$ to let $\Delta u^{\text{p.u.}}_{\text{ins}} = 0$. At this time, the submodules in the same bridge-arm have the same maximum voltages

$$\begin{cases} \left|u^{\text{p.u.}}_{\text{ins,p}i}\right|^{C_{\text{H}}=\frac{1}{2}C_{\text{SW}}}_{\substack{\max \\ (i=1,2,\cdots,N)}} = \frac{N}{2} + \frac{2}{3} + \frac{1}{2}\left(\frac{C_{\text{O}} - 2C_{\text{C}}}{C_{\text{SW}} + C_{\text{H}}}\right) \\ \left|u^{\text{p.u.}}_{\text{ins,n}j}\right|^{C_{\text{H}}=\frac{1}{2}C_{\text{SW}}}_{\substack{\max \\ (j=1,2,\cdots,N)}} = \frac{N}{2} + \frac{2}{3} + \frac{1}{2}\left(\frac{C_{\text{O}} - 2C_{\text{E}}}{C_{\text{SW}} + C_{\text{H}}}\right). \end{cases} \tag{20}$$

As C_{H} continues to increase, the maximum IGBT insulation voltages increase and finally converge on

$$\begin{cases} \left|u^{\text{p.u.}}_{\text{ins,p}i}\right|^{C_{\text{H}}\to\infty}_{\max} = i + \frac{N}{2} \\ \left|u^{\text{p.u.}}_{\text{ins,n}j}\right|^{C_{\text{H}}\to\infty}_{\max} = m + \frac{N}{2}. \end{cases} \tag{21}$$

When $0 < C_{\text{H}} < 0.5C_{\text{SW}}$, the maximum IGBT insulation voltage increases as the submodule gets closer to dc buses. Hence, SM$_{\text{p}1}$ has the largest $|u^{\text{p.u.}}_{\text{ins}}|_{\max}$ in the upper bridge-arm, and SM$_{\text{n}N}$ has the largest $|u^{\text{p.u.}}_{\text{ins}}|_{\max}$ in the lower bridge-arm. When $C_{\text{H}} > 0.5C_{\text{SW}}$, the maximum IGBT insulation voltage decreases as the submodule gets closer to dc buses. At this time, SM$_{\text{p}N}$ has the largest $|u^{\text{p.u.}}_{\text{ins}}|_{\max}$ in the upper bridge-arm, and SM$_{\text{n}1}$ has the largest $|u^{\text{p.u.}}_{\text{ins}}|_{\max}$ in the lower bridge-arm.

The upper boundaries of Fig. 8 forms the safe operation boundaries (SOB) of IGBTs. During the operating process of MMC, the insulation voltages of IGBTs are not allowed to exceed the SOBs. The SOB curves can be used to design the maximum heatsink-to-ground capacitance.

V. SIMULATION AND EXPERIMENT VERIFICATION

To verify the accuracy of (14) and (15), five sets of simulations and experiments are conducted under different values of C_{H}.

TABLE IV
SIMULATION PARAMETERS AND CIRCUIT COMPONENT MODELS

Symbol or Model	Description	Value
U_{dc}	DC voltage	750 V
U_C	Submodule capacitor voltage	187.5 V
N	Bridge-arm submodule amount	4
M	Modulation ratio	0.9
f_r	Fundamental frequency	50 Hz
f_c	Carrier frequency	1 kHz
θ	Carrier phase shift	180°/N
C_H	Heatsink-to-ground capacitance	0/500/1100/ 11000/∞ pF
	Submodule capacitor	C_{SM} = 1 mF R_{CSM} = 190 mΩ L_{CSM} = 735 nH
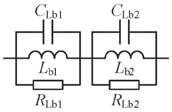	Bridge-arm inductor	L_{b1} = 10 mH L_{b2} = 6.1 μH C_{Lb1} = 645 pF C_{Lb2} = 382 pF R_{Lb1} = 181 kΩ R_{Lb2} = 560 Ω
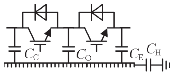	IGBT module (basic dynamic model)	C_C = 140 pF C_O = 175 pF C_E = 35 pF
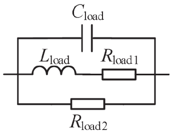	AC load (each phase)	L_{load} = 10 μH R_{load1} = 100 Ω R_{load1} = 4716 Ω C_{load} = 20 pF

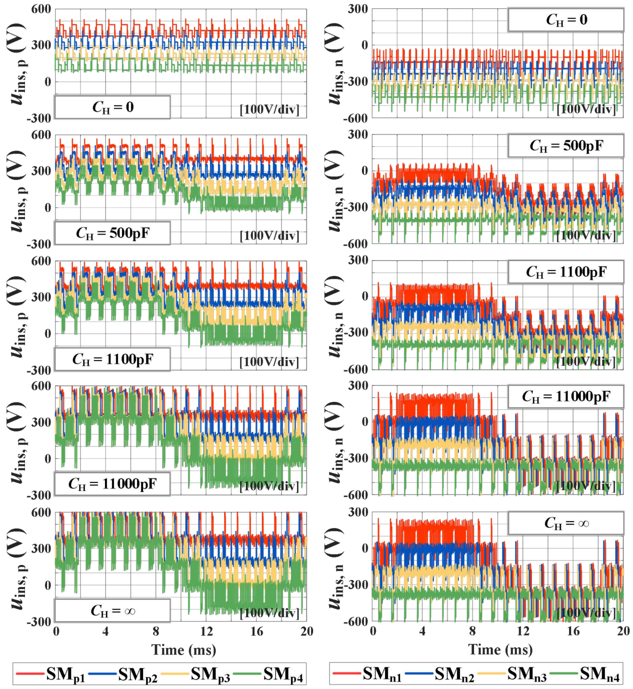

(a) (b)

Fig. 9. Simulation waveforms of IGBT insulation voltages. (a) Upper bridge-arm submodules. (b) Lower bridge-arm submodules.

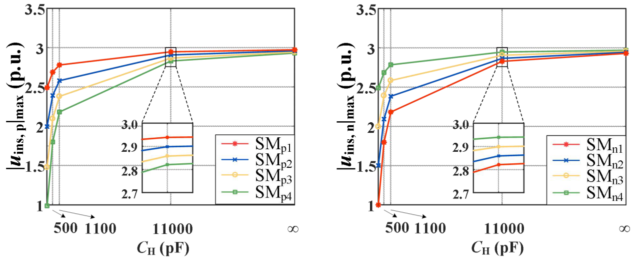

(a) (b)

Fig. 10. Maximum IGBT insulation voltages in simulations. (a) Upper bridge-arm submodules. (b) Lower bridge-arm submodules.

A. *Simulation Measurement Results*

Five sets of simulations are conducted in the simulation software ANSYS Simplorer. The basic simulation parameters and the circuit component models are all listed in Table IV. The adopted modulation method is the CPS-PWM, with the phase shift of two adjacent carriers as $180°/N$.

In the component library of ANSYS Simplorer, there are static and dynamic models for IGBTs and diodes. Different to static models, the dynamic models can reflect the ns-level switching transient processes and the intrinsic parameters can be modified. To simplify the simulations, the adopted switches are the default dynamic models. Moreover, the high frequency parameters of circuit components are also considered. The high frequency parameters are obtained by actual impedance measurement. There is no component model for heatsinks in the component library, so the heatsink of each submodule is represented by the crossing point of C_C, C_O, C_E, and C_H.

Fig. 9 demonstrates the simulation waveforms of IGBT insulation voltages during a fundamental cycle. It can be seen from Fig. 9 that the submodule closer to dc buses has larger IGBT insulation voltage. Therefore, SM_{p1} and SM_{nN} are the most dangerous submodules to break down.

Fig. 10 shows the relation of the simulated maximum IGBT insulation voltages and the heatsink-to-ground capacitance C_H. It can be observed that the IGBT insulation voltages increase as C_H increases. This result agrees with the aforementioned analysis. However, the maximum IGBT insulation voltages in Fig. 10 are smaller than those in Fig. 8. This is because the SOBs in Fig. 8 are the upper limits of IGBT insulation voltages, and the extreme switching-states in Fig. 7 do not appear in the adopted CPS-PWM. The appeared switching-states in simulations and the detailed values of IGBT insulation voltages will be listed at the ending of this section.

B. *Experiment Measurement Results*

Five sets of experiments are conducted in a three-phase MMC prototype. The modulation method is the CPS-PWM. The parameters of experiment conditions are listed in Table V.

The experiment setup is shown in Fig. 11. The dc linear impedance stabilization network is used to isolate the EMI of the dc source. The control system includes a TMS320F28335 DSP central controller for modulation wave generation and three

TABLE V
PARAMETERS OF EXPERIMENT CONDITIONS

Symbol	Description	Value
U_{dc}	DC voltage	750 V
U_{C}	Submodule capacitor voltage	187.5 V
N	Bridge-arm submodule amount	4
M	Modulation ratio	0.9
f_{r}	Fundamental frequency	50 Hz
f_{c}	Carrier frequency	1 kHz
θ	Carrier phase shift	180°/N
C_{SM}	Submodule capacitor	1 mF
L_{b}	Bridge-arm inductor	10 mH
P_{load}	AC load power	1.5 kW
C_{H}	Heatsink-to-ground capacitance	0/500/1100/ 11000/∞ pF

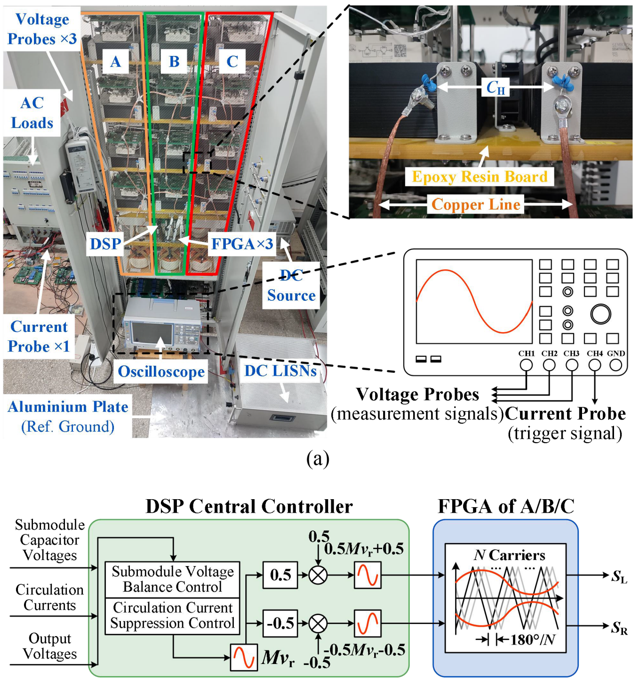

(a)

(b)

Fig. 11. Experiment setup. (a) Prototype. (b) Control and drive manners.

FPGAs for PWM pulse generation. The drivers receive the pulses and then output driver signals to the SKM100GB12 V IGBT modules. Since the used oscilloscope (Rohde&Schwarz RTE1024) has only four channels, it is impossible to measure all insulation voltages at the same time. Thus, the trigger function of the oscilloscope is used for data alignment. The channels are connected with three high voltage differential probes (Keysight N2891A) and one current probe (Rohde&Schwarz RT-ZC10). The current probe measures the output current of Phase A, which acts as the trigger signal.

As shown in Fig. 11(a), the heatsinks are all installed on insulating epoxy resin boards, thus, the heatsinks can be seen as fully floating to the grounded chassis (i.e., $C_{\mathrm{H}} = 0$). The heatsink-to-ground capacitance C_{H} is changed by inserting different ceramic capacitors between the heatsink and the metal chassis. When the heatsinks are directly connected to the chassis by the copper lines $C_{\mathrm{H}} = \infty$.

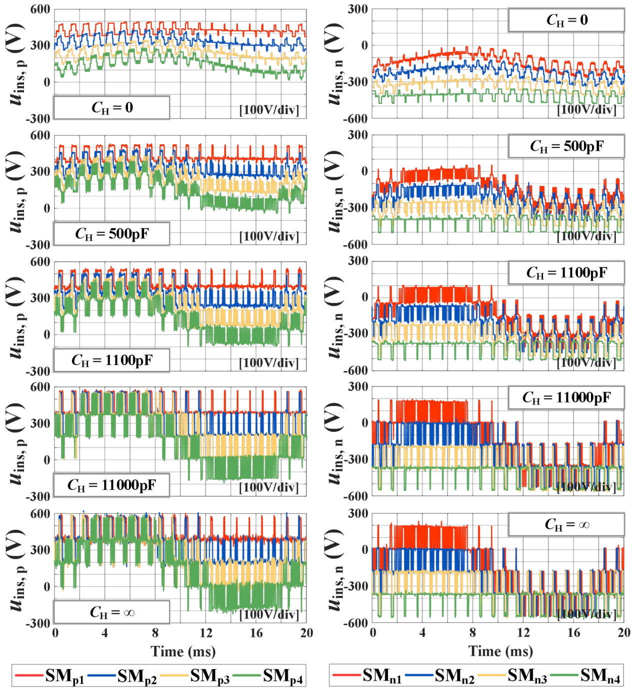

(a) (b)

Fig. 12. Experiment waveforms of IGBT insulation voltages. (a) Upper bridge-arm submodules. (b) Lower bridge-arm submodules.

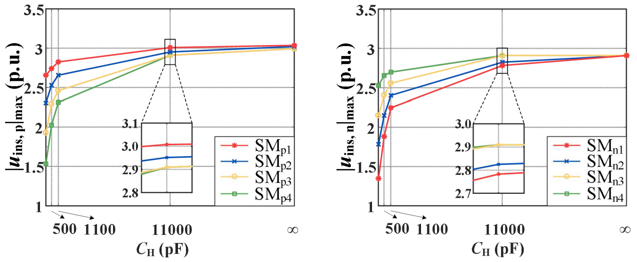

(a) (b)

Fig. 13. Maximum IGBT insulation voltages in experiments. (a) Upper bridge-arm submodules. (b) Lower bridge-arm submodules.

The experiment waveforms are shown in Fig. 12. It can be observed that the submodule closest to the dc buses has the maximum IGBT insulation voltages. Therefore, $\mathrm{SM}_{\mathrm{p1}}$ and $\mathrm{SM}_{\mathrm{n}N}$ are the most dangerous submodules. Most waveforms in Fig. 12 are similar to simulations except the case when $C_{\mathrm{H}} = 0$. The difference is caused by the self-contained stray capacitor of the voltage probe. The voltage probe brings in an equivalent heatsink-to-ground capacitor when it connects to the circuit.

Fig. 13 shows the relation of the maximum IGBT insulation voltages and C_{H} in experiments. It can be seen that the IGBT insulation voltage increases as C_{H} increases. The maximum IGBT insulation voltages in Fig. 13 are smaller than those in Fig. 8. This is because the SOBs in Fig. 8 are the upper limits

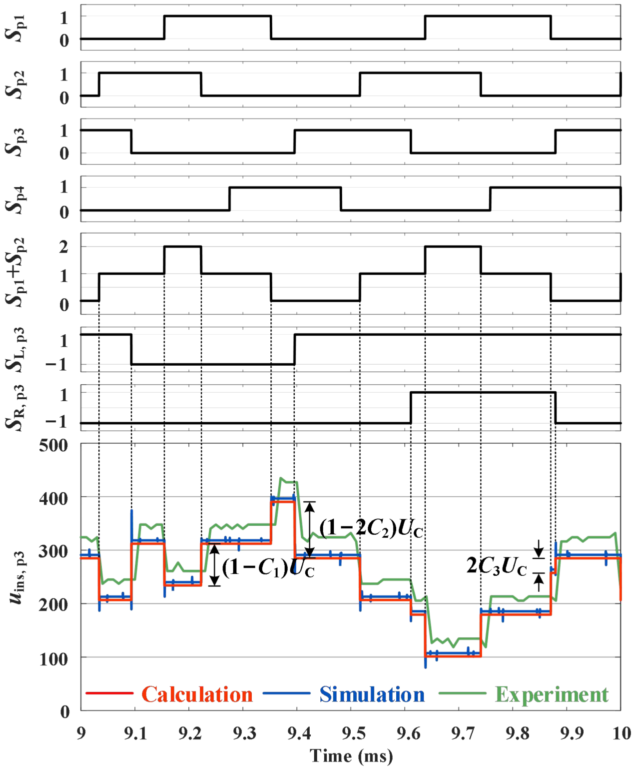

Fig. 14. Detailed submodule switching-states and IGBT insulation voltage waveforms of $\mathrm{SM_{p3}}$ ($C_\mathrm{H} = 500$ pF).

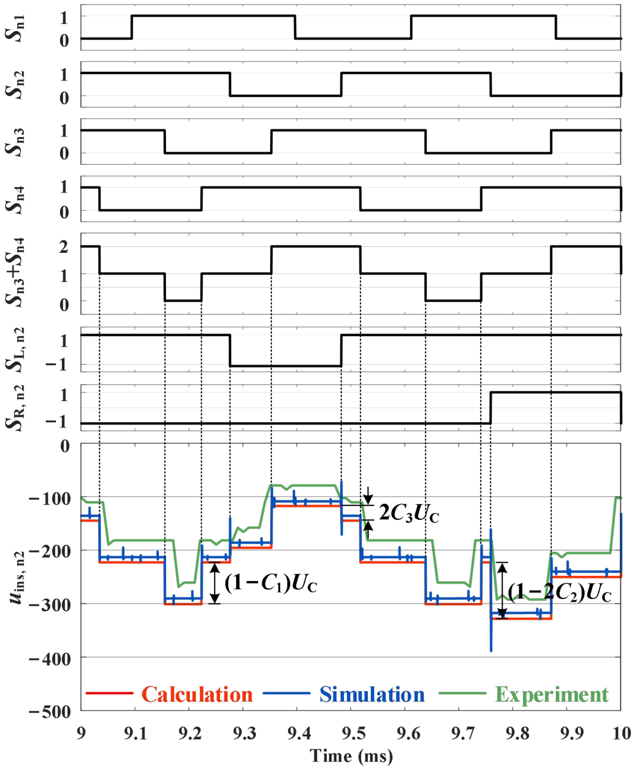

Fig. 15. Detailed submodule switching-states and IGBT insulation voltage waveforms of $\mathrm{SM_{n2}}$ ($C_\mathrm{H} = 500$ pF).

of IGBT insulation voltages. The extreme switching-states in Fig. 7 do not appear in the adopted CPS-PWM. The appeared switching-states in experiments and the corresponding IGBT insulation voltages will be listed at the ending of this section.

C. *Accuracy Verification of Proposed Calculation Method*

The simulation and experiment results shown in Figs. 9 and 12 only demonstrate the overall characteristics of IGBT insulation voltages. Figs. 14 and 15 show the detailed submodule switching-states and IGBT insulation voltage waveforms of $\mathrm{SM_{p3}}$ and $\mathrm{SM_{n2}}$ when $C_\mathrm{H} = 500$ pF. The voltage jumps and the instantaneous voltages of the simulation and experiment results accord with the calculation result well. The voltage jumps are only related to the switching-states of the observed submodule and the submodules closer to dc buses.

To further verify the accuracy of the proposed method, the data comparisons of these results are given in Tables VI and VII. According to Tables VI and VII, it can be concluded that the accuracy of the proposed method is very high. Most of the relative errors are less than 5% (calculation versus simulation) and 20% (calculation versus experiment). The relative errors of calculation and experiment results are caused by the voltage fluctuations of submodule capacitors and the capacitance deviations of the inserted ceramic capacitors. The voltage fluctuations of submodule capacitors in experiments are about 10%. In practical engineering MMCs, the capacitance of submodule capacitors is

TABLE VI
CALCULATION, SIMULATION, AND EXPERIMENT RESULTS OF $\mathrm{SM_{P3}}$

Submodule Switching-states		IGBT insulation voltage $u_{\mathrm{ins,\,p3}}$		
(S_{p1}, S_{p2}, S_{p3}, S_{p4})	($S_{L,p3}$, $S_{R,p3}$)	Cal. (V)	Sim. (V)	Exp. (V)
(0, 0, 0, 0)	(1, 1)	257.42	263.67	292.49
	(−1, −1)	390.23	396.52	426.88
(0, 0, 0, 1)	(1, 1)	257.42	263.67	292.49
	(−1, −1)	390.23	396.52	426.88
(0, 0, 1, 0)	(1, −1)	284.77	291.14	316.21
(0, 0, 1, 1)	(1, −1)	284.77	291.14	316.21
(0, 1, 0, 0)	(1, 1)	179.30	185.62	213.44
	(−1, −1)	312.11	318.30	347.83
(0, 1, 0, 1)	Switching-state does not appear.			
(0, 1, 1, 0)	(1, −1)	206.64	212.93	237.15
(0, 1, 1, 1)	(1, −1)	206.64	212.93	237.15
(1, 0, 0, 0)	(1, 1)	179.30	185.62	213.44
	(−1, −1)	312.11	318.30	347.83
(1, 0, 0, 1)	(1, 1)	179.30	185.62	213.44
	(−1, −1)	312.11	318.30	347.83
(1, 0, 1, 0)	Switching-state does not appear.			
(1, 0, 1, 1)	(1, −1)	206.64	212.93	237.15
(1, 1, 0, 0)	(1, 1)	101.17	107.38	126.48
	(−1, −1)	233.98	240.15	260.87
(1, 1, 0, 1)	(1, 1)	101.17	107.38	126.48
	(−1, −1)	233.98	240.15	260.87
(1, 1, 1, 0)	(1, −1)	128.52	139.73	158.10
(1, 1, 1, 1)	(1, −1)	128.52	139.73	158.10

TABLE VII
CALCULATION, SIMULATION, AND EXPERIMENT RESULTS OF $\mathrm{SM}_{\mathrm{N2}}$

Submodule Switching-states		IGBT insulation voltage $u_{\mathrm{ins,\,n2}}$		
(S_{n1}, S_{n2}, S_{n3}, S_{n4})	($S_{L,\,n2}$, $S_{R,\,n2}$)	Cal. (V)	Sim. (V)	Exp. (V)
(0, 0, 0, 0)	(1, 1)	–406.64	–395.32	–379.45
	(–1, –1)	–273.83	–263.38	–245.06
(0, 0, 0, 1)	(1, 1)	–328.52	–316.57	–300.40
	(–1, –1)	–195.70	–185.74	–166.01
(0, 0, 1, 0)	(1, 1)	–328.52	–316.57	–300.40
	(–1, –1)	–195.70	–185.73	–166.01
(0, 0, 1, 1)	(1, 1)	–250.39	–244.07	–229.25
	(–1, –1)	–117.58	–112.53	–79.05
(0, 1, 0, 0)	(1, –1)	–301.17	–290.48	–268.77
(0, 1, 0, 1)	Switching-state does not appear.			
(0, 1, 1, 0)	(1, –1)	–223.05	–216.56	–205.53
(0, 1, 1, 1)	(1, –1)	–144.92	–138.70	–118.58
(1, 0, 0, 0)	(1, 1)	–406.64	–395.32	–379.45
	(–1, –1)	–273.83	–263.38	–245.06
(1, 0, 0, 1)	(1, 1)	–328.52	–316.57	–300.40
	(–1, –1)	–195.70	–185.73	–166.01
(1, 0, 1, 0)	Switching-state does not appear.			
(1, 0, 1, 1)	(1, 1)	–250.39	–244.07	–229.25
	(–1, –1)	–117.58	–112.53	–79.05
(1, 1, 0, 0)	(1, –1)	–301.17	–290.48	–268.77
(1, 1, 0, 1)	(1, –1)	–223.05	–216.56	–205.53
(1, 1, 1, 0)	(1, –1)	–223.05	–216.56	–205.53
(1, 1, 1, 1)	(1, –1)	–144.92	–138.70	–118.58

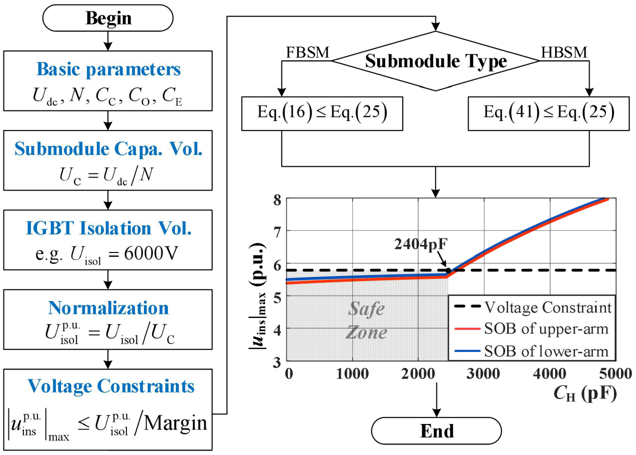

Fig. 16. Design steps of the maximum heatsink-to-ground capacitance.

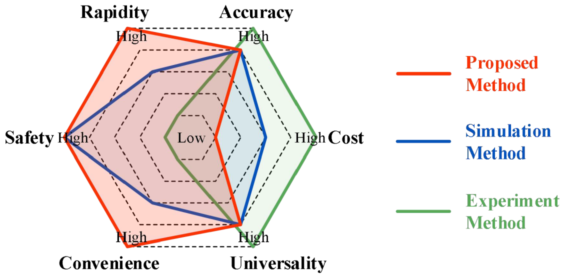

Fig. 17. Performance comparison of different methods.

greater than that of the experiment prototype. Therefore, the proposed calculation method has higher accuracy in practical engineering MMCs.

It can also been observed in Tables VI and VII that not all switching-states appear in the adopted CPS-PWM. The reversed-ON-state never appears in the conducted simulations and experiments. This result explains why the maximum IGBT insulation voltages in Figs. 10 and 13 are lower than the SOBs in Fig. 8.

VI. APPLICATION: DESIGN OF THE MAXIMUM HEATSINK-TO-GROUND CAPACITANCE

To ensure the absolute insulation safety of IGBT modules, it is necessary to limit the heatsink-to-ground capacitance C_{H}. The detailed design steps are as follows.

A. *Calculate Submodule Capacitor Average Voltage* U_{C}

Take a 10 kV MMC as an example. In this MMC, there are 10 FBSMs in each bridge-arm. The average voltage of the submodule capacitors can, then, be calculated as

$$U_{\mathrm{C}} = \frac{10\mathrm{kV}}{10} = 1000\mathrm{V}. \tag{22}$$

B. *Look Up IGBT Isolation Voltage* U_{isol} *in User Manual*

To avoid insulation breakdown, the insulation voltage of an IGBT can not exceed its isolation voltage. The isolation voltage of an IGBT is usually given in its user manual. For example, the user manual of ABBSS03257 IGBT Discrete (3300 V/1500 A) gives the IGBT isolation voltage as

$$U_{\mathrm{isol}} = 6000\mathrm{V}. \tag{23}$$

The IGBT isolation voltage p.u. value is then calculated as

$$U_{\mathrm{isol}}^{\mathrm{p.u.}} = \frac{U_{\mathrm{isol}}}{U_{\mathrm{C}}} = \frac{6000\mathrm{V}}{1000\mathrm{V}} = 6. \tag{24}$$

Considering that there are 5% fluctuations on submodule capacitor voltages, a 1.05 times margin should be reserved

$$|u_{\mathrm{ins}}^{\mathrm{p.u.}}|_{\mathrm{max}} \le \frac{U_{\mathrm{isol}}^{\mathrm{p.u.}}}{1.05} = \frac{600}{105}. \tag{25}$$

C. *Design Maximum Heatsink-to-Ground Capacitance* C_{H}

According to Fig. 8, $\mathrm{SM}_{\mathrm{p1}}$ and $\mathrm{SM}_{\mathrm{n}N}$ are the most dangerous submodules when $0 < C_{\mathrm{H}} < 0.5C_{\mathrm{SW}}$, while $\mathrm{SM}_{\mathrm{p}N}$ and $\mathrm{SM}_{\mathrm{n1}}$ are the most dangerous submodules when $C_{\mathrm{H}} > 0.5C_{\mathrm{SW}}$. Based on (16), the voltage constraints are calculated by

$$\begin{cases} \left|u_{\mathrm{ins,p1}}^{\mathrm{p.u.}}\right|_{\substack{\mathrm{max} \\ 0<C_{\mathrm{H}}<0.5C_{\mathrm{SW}}}} = -\frac{1}{2}C_1 + 1 + \frac{N}{2} + \frac{1}{2}\left(\frac{C_{\mathrm{O}}-2C_{\mathrm{C}}}{C_{\mathrm{SW}}+C_{\mathrm{H}}}\right) \le \frac{600}{105} \\ \left|u_{\mathrm{ins,n}N}^{\mathrm{p.u.}}\right|_{\substack{\mathrm{max} \\ 0<C_{\mathrm{H}}<0.5C_{\mathrm{SW}}}} = -\frac{1}{2}C_1 + 1 + \frac{N}{2} + \frac{1}{2}\left(\frac{C_{\mathrm{O}}-2C_{\mathrm{E}}}{C_{\mathrm{SW}}+C_{\mathrm{H}}}\right) \le \frac{600}{105} \end{cases} \tag{26}$$

$$\begin{cases} \left|u_{\mathrm{ins,p}N}^{\mathrm{p.u.}}\right|_{\substack{\max \\ C_{\mathrm{H}}>0.5C_{\mathrm{SW}}}} = \left(1-\frac{3N}{2}\right)C_1+\frac{3N}{2}+\frac{1}{2}\left(\frac{C_{\mathrm{O}}-2C_{\mathrm{C}}}{C_{\mathrm{SW}}+C_{\mathrm{H}}}\right) \le \frac{600}{105} \\ \left|u_{\mathrm{ins,n1}}^{\mathrm{p.u.}}\right|_{\substack{\max \\ C_{\mathrm{H}}>0.5C_{\mathrm{SW}}}} = \left(1-\frac{3N}{2}\right)C_1+\frac{3N}{2}+\frac{1}{2}\left(\frac{C_{\mathrm{O}}-2C_{\mathrm{E}}}{C_{\mathrm{SW}}+C_{\mathrm{H}}}\right) \le \frac{600}{105}. \end{cases} \tag{27}$$

For an ABBSS03257 IGBT Discrete, its stray capacitance C_{C} is measured as 809 pF and C_{E} is 386 pF [30]. When two IGBT Discretes form a half-bridge, the stray capacitance C_{O} is the sum of C_{C} and C_{E}, i.e., $C_{\mathrm{O}} = 1195$ pF. Substitute C_{C}, C_{O}, C_{E} into (26) and (27), the heatsink-to-ground capacitance is limited as

$$C_{\mathrm{H}} \le 2404\mathrm{pF}. \tag{28}$$

That is to say, the heatsink-to-ground capacitance C_{H} can not be larger than 2404 pF. This capacitance value is so small that the heatsinks are almost floating to the ground. Fig. 16 gives the flow chart of the design steps. If the MMC is not working in over-modulation mode, the maximum heatsink-to-ground capacitance can be bigger than (28). At this time, the voltage constraints (26) and (27) are replaced by (17).

VII. CONCLUSION

To assess the IGBT insulation voltages in MMC, this article proposes a calculation method based on the switching-states and stray capacitors of submodules. The proposed method can calculate the IGBT insulation voltages accurately, with most of the relative errors less than 5% (calculation versus simulation) and 20% (calculation versus experiment). The contributions, benefits and limitation of the proposed method are as follows.

1) The proposed method gives a comprehensive analysis on the IGBT insulation voltages in MMC. The IGBT insulation voltages are relevant to the submodule switching-states, the heatsink-to-ground capacitance, the amount of submodules, and the submodule locations. Under normal conditions, $\mathrm{SM}_{\mathrm{p1}}$ and $\mathrm{SM}_{\mathrm{n}N}$ are the most possible submodules to insulation break down.
2) This article also gives the safe operation boundaries of IGBT insulation voltages in MMC. The analysis shows that the maximum IGBT insulation voltages increase as C_{H} increases. To ensure the safety of IGBTs, the heatsinks should be floating to the ground as possible.
3) Compared to the existing methods, the proposed method is more convenient to use. Most of the used parameters are the basic parameters of MMC. Only one offline measurement of the stray capacitance is needed [31].
4) The proposed method is based on the heatsink structure show in Fig. 4. In some MMCs, the heatsinks are not this structure, so the proposed method is not applicable [32].

Fig. 17 shows the performance comparison of the proposed method and the simulation and experiment methods.

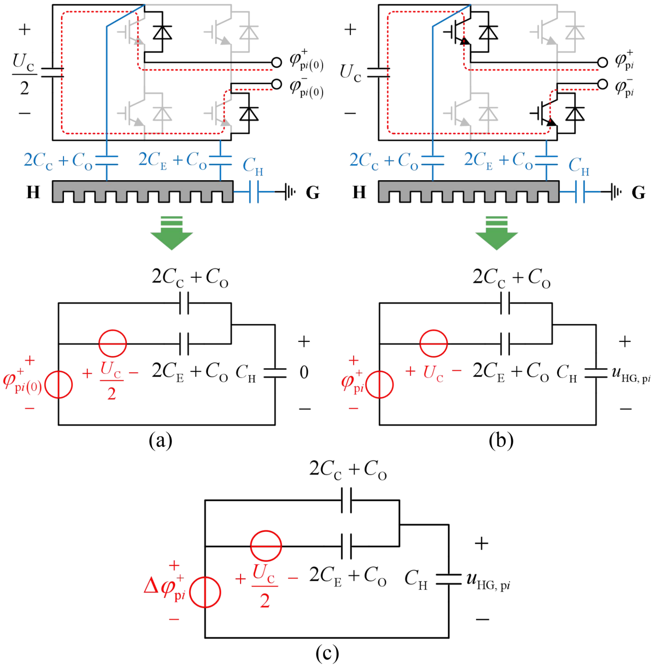

Fig. 18. Equivalent circuit of FBSM. (a) When $S_{\mathrm{p1}} = S_{\mathrm{p2}} = \ldots = S_{\mathrm{p}N} = 0$. (b) When $S_{\mathrm{p1}} = S_{\mathrm{p2}} = \ldots = S_{\mathrm{p}N} = 1$. (c) Superposition of (a) and (b).

APPENDIX

A. *Derivation of FBSMs (Full-Bridge Mode)*

The time derivatives of $u_{\mathrm{HG,\ p}i}^{\mathrm{p.u.}}$ and $u_{\mathrm{HG,\ n}j}^{\mathrm{p.u.}}$ are

$$\begin{cases} \frac{\mathrm{d}}{\mathrm{d}t}\left(\frac{u_{\mathrm{HG,p}i}}{U_{\mathrm{C}}}\right) = -C_1\frac{\mathrm{d}}{\mathrm{d}t}\left(\sum_{k=1}^{i-1}S_{\mathrm{p}k}\right) - C_2\frac{\mathrm{d}S_{\mathrm{L,p}i}}{\mathrm{d}t} + C_3\frac{\mathrm{d}S_{\mathrm{R,p}i}}{\mathrm{d}t} \\ \frac{\mathrm{d}}{\mathrm{d}t}\left(\frac{u_{\mathrm{HG,n}j}}{U_{\mathrm{C}}}\right) = C_1\frac{\mathrm{d}}{\mathrm{d}t}\left(\sum_{l=j+1}^{N}S_{\mathrm{n}l}\right) + C_3\frac{\mathrm{d}S_{\mathrm{L,n}j}}{\mathrm{d}t} - C_2\frac{\mathrm{d}S_{\mathrm{R,n}j}}{\mathrm{d}t}. \end{cases} \tag{29}$$

Integrate (29), then

$$\begin{cases} u_{\mathrm{HG,p}i}^{\mathrm{p.u.}} = -C_1\sum_{k=1}^{i-1}S_{\mathrm{p}k} - C_2S_{\mathrm{L,p}i} + C_3S_{\mathrm{R,p}i} + K_{\mathrm{p}i} \\ u_{\mathrm{HG,n}j}^{\mathrm{p.u.}} = C_1\sum_{l=j+1}^{N}S_{\mathrm{n}l} + C_3S_{\mathrm{L,n}j} - C_2S_{\mathrm{R,n}j} + L_{\mathrm{n}j} \end{cases} \tag{30}$$

where $K_{\mathrm{p}i}$ and $L_{\mathrm{n}j}$ are integration constants. Once any solution of (30) is known, $K_{\mathrm{p}i}$ and $L_{\mathrm{n}j}$ can then be determined.

When the IGBTs are all turned OFF, the heatsink-to-ground voltages are all zero. In this case, the MMC is in uncontrolled rectifier state, and the equivalent circuit of FBSM can be drawn as Fig. 18(a). Fig. 18(b) shows the equivalent circuit of FBSM when $S_{\mathrm{p1}} = S_{\mathrm{p2}} = \ldots = S_{\mathrm{p}N} = 1$. Obviously, the circuit in Fig. 18(b) can be seen as the superposition of the circuits in Fig. 18(a) and (c), where

$$\varphi_{\mathrm{p}i(0)}^{+} = \frac{U_{\mathrm{dc}}}{2} - (i-1)\frac{U_{\mathrm{C}}}{2} \tag{31}$$

$$\varphi_{\mathrm{p}i}^{+} = \frac{U_{\mathrm{dc}}}{2} - (i-1)U_{\mathrm{C}} \tag{32}$$

$$\Delta\varphi_{\mathrm{p}i}^{+} = \varphi_{\mathrm{p}i}^{+} - \varphi_{\mathrm{p}i(0)}^{+} = -(i-1)\frac{U_{\mathrm{C}}}{2}. \tag{33}$$

In Fig. 18(c), the heatsink-to-ground voltages are

$$u_{\mathrm{HG,p}i} = \frac{C_{\mathrm{SW}}}{C_{\mathrm{SW}} + C_{\mathrm{H}}} \Delta\varphi_{\mathrm{p}i}^{+} - \frac{2C_{\mathrm{E}} + C_{\mathrm{O}}}{C_{\mathrm{SW}} + C_{\mathrm{H}}} \frac{U_{\mathrm{C}}}{2}. \tag{34}$$

Substitute (33) into (34), then

$$u_{\mathrm{HG,p}i}^{\mathrm{p.u.}} = -\frac{i-1}{2} C_1 - C_4 \tag{35}$$

where $C_4 = \frac{1}{2} \frac{2C_{\mathrm{E}}+C_{\mathrm{O}}}{C_{\mathrm{SW}}+C_{\mathrm{H}}}$.

According to (30), when $S_{\mathrm{p1}} = S_{\mathrm{p2}} = \ldots\ = S_{\mathrm{p}N} = 1$, the heatsink-to-ground voltages can also be calculated by

$$u_{\mathrm{HG,p}i}^{\mathrm{p.u.}} = -C_1 (i-1) - C_2 - C_3 + K_{\mathrm{p}i}. \tag{36}$$

By comparing (35) and (36), the integration constant $K_{\mathrm{p}i}$ can be obtained as

$$K_{\mathrm{p}i} = \frac{i}{2} C_1 - C_4. \tag{37}$$

The integration constant $L_{\mathrm{n}j}$ can be obtained by the similar ways of $K_{\mathrm{p}i}$, and the result is as

$$L_{\mathrm{n}j} = -\frac{(N-j)}{2} C_1 - C_4. \tag{38}$$

B. Derivations of FBSMs (Half-Bridge Mode) and HBSMs

When an FBSM works in half-bridge mode, its T_3 keeps OFF and T_4 keeps ON. Therefore

$$S_{\mathrm{R}} = S_3 - S_4 \equiv -1. \tag{39}$$

Substitute (39) into (14), (15), then

$$\begin{cases} u_{\mathrm{ins,p}i}^{\mathrm{p.u.}} = u_{\mathrm{1G,p}i}^{\mathrm{p.u.}} - u_{\mathrm{HG,p}i}^{\mathrm{p.u.}} \\ \quad = (C_1 - 1) \sum_{k=1}^{i-1} S_{\mathrm{p}k} + \left(C_2 - \frac{1}{2}\right) S_{\mathrm{L,p}i} - \frac{i}{2} C_1 \\ \quad\ + \frac{N+1}{2} + C_3 + C_4 \\ u_{\mathrm{ins,n}j}^{\mathrm{p.u.}} = u_{\mathrm{3G,n}j}^{\mathrm{p.u.}} - u_{\mathrm{HG,p}i}^{\mathrm{p.u.}} \\ \quad = (1 - C_1) \sum_{l=j+1}^{N} S_{\mathrm{n}l} - C_3 S_{\mathrm{L,n}j} + \frac{m}{2} C_1 \\ \quad\ - \frac{N}{2} - C_2 - C_5 \end{cases} \tag{40}$$

where $m = N - j + 1$ and $C_5 = \frac{1}{2} \frac{2C_{\mathrm{C}}+C_{\mathrm{O}}}{C_{\mathrm{SW}}+C_{\mathrm{H}}}$.

When $S_{\mathrm{p1}} = S_{\mathrm{p2}} = \ldots\ = S_{\mathrm{p}(i-1)} = 0$ and $S_{\mathrm{L,\ p}i} = -1$, $|u_{\mathrm{ins,\ p}i}^{\mathrm{p.u.}}|$ has its maximum value; when $S_{\mathrm{n}(j+1)} = S_{\mathrm{n}(j+2)} = \ldots = S_{\mathrm{n}N} = 0$ and $S_{\mathrm{L,\ n}j} = 1$, $|u_{\mathrm{ins,\ p}i}^{\mathrm{p.u.}}|$ has its maximum value. The maximum IGBT insulation voltages are calculated as

$$\begin{cases} \left| u_{\mathrm{ins,p}i}^{\mathrm{p.u.}} \right|_{\max} = \frac{N+2}{2} - \frac{i}{2} C_1 - C_2 + C_3 + C_4 \\ \left| u_{\mathrm{ins,n}j}^{\mathrm{p.u.}} \right|_{\max} = \frac{N}{2} - \frac{m}{2} C_1 + C_2 + C_3 + C_5. \end{cases} \tag{41}$$

When the submodules are HBSMs, the voltage expressions are the same to (40) and (41). The only one difference is that the values of C_1–C_5 and C_{SW} in HBSMs are different with those in FBSMs. The detailed values of the stray capacitance are listed in Table VIII.

TABLE VIII
STRAY CAPACITANCE OF FBSM AND HBSM

Symbol	Value (FBSM)	Value (HBSM)
C_1	$\frac{C_{\mathrm{SW}}}{C_{\mathrm{SW}} + C_{\mathrm{H}}}$	
C_2	$\frac{1}{2} \frac{C_{\mathrm{SW}} - C_{\mathrm{O}}}{C_{\mathrm{SW}} + C_{\mathrm{H}}}$	
C_3	$\frac{1}{2} \frac{C_{\mathrm{O}}}{C_{\mathrm{SW}} + C_{\mathrm{H}}}$	
C_4	$\frac{1}{2} \frac{2C_{\mathrm{E}} + C_{\mathrm{O}}}{C_{\mathrm{SW}} + C_{\mathrm{H}}}$	$\frac{1}{2} \frac{C_{\mathrm{E}}}{C_{\mathrm{SW}} + C_{\mathrm{H}}}$
C_5	$\frac{1}{2} \frac{2C_{\mathrm{C}} + C_{\mathrm{O}}}{C_{\mathrm{SW}} + C_{\mathrm{H}}}$	$\frac{1}{2} \frac{C_{\mathrm{C}} + C_{\mathrm{O}}}{C_{\mathrm{SW}} + C_{\mathrm{H}}}$
C_{SW}	$2\left(C_{\mathrm{C}} + C_{\mathrm{O}} + C_{\mathrm{E}}\right)$	$C_{\mathrm{C}} + C_{\mathrm{O}} + C_{\mathrm{E}}$

REFERENCES

[1] A. Lesnicar and R. Marquardt, “An innovative modular multilevel converter topology suitable for a wide power range,” in *Proc. IEEE Bologna Power Tech Conf.*, Bologna, Italy, 2003, vol. 3, pp. 6–11.

[2] H. Lin, H. S.-H. Chung, R. Shen, and Y. Xiang, “Enhancing stability of DC cascaded systems with CPLs using MPC combined with NI and accounting for parameter uncertainties,” *IEEE Trans. Power Electron.*, vol. 39, no. 5, pp. 5225–5238, May 2024.

[3] Y. Xiang, H. S.-H. Chung, and H. Lin, “Light implementation scheme of ANN-based explicit model-predictive control for DC-DC power converters,” *IEEE Trans. Ind. Inform.*, vol. 20, no. 3, pp. 4065–4078, Mar. 2024.

[4] M. A. Perez, S. Bernet, J. Rodriguez, S. Kouro, and R. Lizana, “Circuit topologies, modeling, control schemes, and applications of modular multilevel converters,” *IEEE Trans. Power Electron.*, vol. 30, no. 1, pp. 4–17, Jan. 2015.

[5] S. Debnath, J. Qin, B. Bahrani, M. Saeedifard, and P. Barbosa, “Operation, control, and applications of the modular multilevel converter: A review,” *IEEE Trans. Power Electron.*, vol. 30, no. 1, pp. 37–53, Jan. 2015.

[6] X. Gong and J. A. Ferreira, “Investigation of conducted EMI in SiC JFET inverters using separated heat sinks,” *IEEE Trans. Power Electron.*, vol. 61, no. 1, pp. 115–125, Jan. 2014.

[7] R. Zhu, N. Lin, V. Dinavahi, and G. Liang, “An accurate and fast method for conducted EMI modeling and simulation of MMC-based HVDC converter station,” *IEEE Trans. Power Electron.*, vol. 35, no. 5, pp. 4689–4702, May 2020.

[8] H. Sun, X. Cui, and L. Du, “EMI prediction of ±800 kV UHVDC converter station,” *IEEE Trans. Magn.*, vol. 52, no. 3, Mar. 2016, Art. no. 9400404.

[9] D. Cottet et al., “Electromagnetic modeling of high voltage multi-level converter substations,” in *Proc. IEEE Int. Symp. Electromagn. Compat. 2018 IEEE Asia-Pacific Symp. Electromagn. Compat.*, Suntec City, Singapore, 2018, pp. 1001–1006.

[10] J. H. Fabian, S. Hartmann, and A. Hamidi, “Analysis of insulation failure modes in high power IGBT modules,” in *Proc. Ind. Appl. Conf.*, Hong Kong, China, 2005, vol. 2, pp. 799–805.

[11] J. Li, Y. Liang, Y. Mei, X. Tang, and G.-Q. Lu, “Packaging design of 15 kV SiC power devices with high-voltage encapsulation,” *IEEE Trans. Dielectrics Elect. Insul.*, vol. 29, no. 1, pp. 47–53, Feb. 2022.

[12] G. Mitic and G. Lefranc, “Localization of electrical-insulation and partial-discharge failures of IGBT modules,” *IEEE Trans. Ind. Appl.*, vol. 38, no. 1, pp. 175–180, Jan./Feb. 2002.

[13] G. Callender et al., “Critical analysis of partial discharge dynamics in air filled spherical voids,” *J. Phys. D, Appl. Phys.*, vol. 51, no. 12, pp. 1–13, 2018.

[14] G. Callender, T. Tanmaneeprasert, and P. L. Lewin, “Simulating partial discharge activity in a cylindrical void using a model of plasma dynamics,” *J. Phys. D, Appl. Phys.*, vol. 52, no. 5, pp. 1–12, 2019.

[15] M. Morshed et al., “High temperature polyimide polymer material for high voltage IGBT power module switching applications,” in *Proc. 20th Eur. Conf. Power Electron. Appl.*, Riga, Latvia, 2018, pp. P1–P7.

[16] M. Sato, A. Kumada, K. Hidaka, K. Yamashiro, Y. Hayase, and T. Takano, “Surface discharges in silicone gel on AlN substrate,” *IEEE Trans. Dielectrics Elect. Insul.*, vol. 23, no. 1, pp. 494–500, Feb. 2016.

[17] P. Fu et al., “Partial discharge measurement and analysis in high voltage IGBT modules under DC voltage,” *CSEE J. Power Energy*, vol. 4, no. 4, pp. 513–523, Dec. 2018.

[18] H. You, Z. Wei, B. Hu, Z. Zhao, R. Na, and J. Wang, “Partial discharge behaviors in power modules under square pulses with ultrafast dv/dt,” *IEEE Trans. Power Electron.*, vol. 36, no. 3, pp. 2611–2620, Mar. 2021.

[19] X. Liu et al., “Characteristics and identification of partial discharge for insulation structures in high voltage IGBT modules under positive square wave voltage,” *IEEE Trans. Power Electron.*, vol. 38, no. 4, pp. 5347–5359, Apr. 2023.

[20] U.-M. Choi, F. Blaabjerg, S. Jørgensen, S. Munk-Nielsen, and B. Rannestad, “Reliability improvement of power converters by means of condition monitoring of IGBT modules,” *IEEE Trans. Power Electron.*, vol. 32, no. 10, pp. 7990–7997, Oct. 2017.

[21] M. A. Rodríguez-Blanco et al., “A failure-detection strategy for IGBT based on gate-voltage behavior applied to a motor drive system,” *IEEE Trans. Ind. Electron.*, vol. 58, no. 5, pp. 1625–1633, May 2011.

[22] Y.-S. Kim and S.-K. Sul, “On-line estimation of IGBT junction temperature using on-state voltage drop,” in *Proc. Ind. Appl. Conf.*, St. Louis, MO, USA, 1998, pp. 853–859.

[23] D. W. Brown, M. Abbas, A. Ginart, I. N. Ali, P. W. Kalgren, and G. J. Vachtsevanos, “Turn-off time as an early indicator of insulated gate bipolar transistor latch-up,” *IEEE Trans. Power Electron.*, vol. 27, no. 2, pp. 479–489, Feb. 2012.

[24] S. Chen, S. Ji, L. Pan, C. Liu, and L. Zhu, “An on-state voltage calculation scheme of MMC submodule IGBT,” *IEEE Trans. Power Electron.*, vol. 34, no. 8, pp. 7996–8007, Aug. 2019.

[25] C. Zhan et al., “A novel sensor-reduction condition monitoring approach for MMC submodule IGBTs based on statistics of inferred on-state voltage,” *IEEE J. Emerg. Sel. Topics Power Electron.*, vol. 12, no. 1, pp. 1068–1077, Feb. 2024.

[26] I. Semenov, I. F. Gunheim, K. Niayesh, H. K. H. Meyer, and L. Lundgaard, “Investigation of partial discharges in AlN substrates under fast transient voltages,” *IEEE Trans. Dielectrics Elect. Insul.*, vol. 29, no. 2, pp. 745–752, Apr. 2022.

[27] S. Dey, A. Mallik, and S. Mishra, “A mathematical design approach to volumetric optimization of EMI filter and modeling of CM noise sources in a three-phase PFC,” *IEEE Trans. Power Electron.*, vol. 37, no. 1, pp. 462–472, Jan. 2022.

[28] T. Sun, X. Pei, Y. Shan, J. Pei, and D. Jiang, “Submodule switching-state based EMI modeling and mixed-mode EMI phenomenon in MMC,” *IEEE Trans. Power Electron.*, vol. 38, no. 2, pp. 1831–1843, Feb. 2023.

[29] Y. Zhang, J. Zhang, F. Deng, Z. Xu, and J. Zhao, “Hybrid modular multilevel converter with self-balancing structure,” *IEEE Trans. Ind. Appl.*, vol. 57, no. 5, pp. 5039–5051, Sep./Oct. 2021.

[30] R. Wang, D. Jiang, J. Chen, and W. Sun, “Conducted EMI analysis and modeling for the main circuit of a MMC submodule,” in *Proc. Asia-Pacific Int. Symp. Electromagn. Compat.*, Beijing, China, 2022, pp. 659–662.

[31] Y. Xiang, X. Pei, W. Zhou, Y. Kang, and H. Wang, “A fast and precise method for modeling EMI source in two-level three-phase converter,” *IEEE Trans. Power Electron.*, vol. 34, no. 11, pp. 10650–10664, Nov. 2019.

[32] R. Wang, Y. Liang, D. Jiang, H. Xiao, and H. Peng, “The near magnetic field measurement and characteristic analysis inside the valve hall of an MMC mutual driving system,” in *Proc. Power Electron. Appl. Conf.*, Guangzhou, China, 2022, pp. 1503–1506.

Tao Sun was born in Jiangxi Province, China, in 1996. He received the B.S. degree in electrical engineering and automation from the School of Electrical and Electronic Engineering, North China Electric Power University, Beijing, China, in 2018. He is currently working toward the Ph.D. degree in electrical engineering with the Huazhong University of Science and Technology, Wuhan, China.

His research interests include the modeling and suppression methods of EMI in power electronic converters.

Xuejun Pei (Senior Member, IEEE) received the B.E., M.E., and Ph.D. degrees in electrical engineering from the Huazhong University of Science and Technology, Wuhan, China, in 1998, 2001, and 2004, respectively.

In 2004, he was with the Huazhong University of Science and Technology as a Teaching Assistant. Since 2006, he has been a Full Professor with the College of Electrical and Electronic Engineering, Huazhong University of Science and Technology. His research interests include high-power converter, EMC issue, fault diagnosis of power electronics, and the related application in the power system.

Jiuqing Cai received the Ph.D. degree in electrical engineering from Huazhong University of Science and Technology, Wuhan, China, in 2017.

Since 2017, he has been an Engineer with the Wuhan Second Ship Design and Research Institute, Wuhan, China. His research interests include ship integrated power system and application of power electronics technology.

Fang Wu received the Ph.D. degree in control science and control engineering from Huazhong University of Science and Technology, Wuhan, China, in 2018.

Since 2018, he has been an Engineer with the Wuhan Second Ship Design and Research Institute, Wuhan, China. His research interests include electrical engineering and automation, and application of power electronics technology.

Youwen Zhang received the B.S. degree in electrical engineering from the School of Electrical Engineering, Chongqing University, Chongqing, China, in 2020.

He is currently working toward the Ph.D. degree in electrical engineering with the Huazhong University of Science and Technology, Wuhan, China. His current research interests include control and protection of ac–dc hybrid distribution network.

Yong Kang (Fellow, IEEE) was born in Hubei, China, in 1965. He received the B.E., M.E., and Ph.D. degrees in electrical engineering from Huazhong University of Science and Technology, Wuhan, China, in 1988, 1991, and 1994, respectively.

Since 1994, he has been a Faculty Member with Huazhong University of Science and Technology, where he is currently a Full Professor with the School of Electrical and Electronic Engineering. His research interests include power electronic converters, ac drivers, and renewable energy generation systems.

Dr. Kang was a recipient of the Delta Scholar Award from the Delta Environmental and Educational Foundation in 2005 and supported by the Program for New Century Excellent Talents in University from the Chinese Ministry of Education in 2004. In 2017, he was appointed as the Chief Scientist of the National Key Research and Development Program of China. He was a recipient of the highly prestigious China National Science and Technology Award in 2019. He currently the Vice Chairperson for the China UPS Standard Committee and an Associate Editor for the *Journal of Power Electronics*.